

## Article

# Sapo-34 Obtained from Amazonian Flint Kaolin: Influence of Impurities of “Oxidized Fe/Ti” in Synthesis and Its Application in the Removal of Cationic Dye from Water

Darllan R. Pinheiro <sup>1,\*</sup>, Alice P. Pinheiro <sup>1</sup>, Fabio A. Pontes <sup>1</sup>, João Vitor K. Soares <sup>2</sup>, Roberto F. Neves <sup>2</sup> and Simone P. A. Paz <sup>1,2</sup>

<sup>1</sup> Programa de Pós-Graduação em Engenharia de Recursos Naturais da Amazônia PRODERNA/ITEC/UFPA, Rua Augusto Correa, 01, Belém 66075-110, PA, Brazil

<sup>2</sup> Faculdade de Engenharia Química FEQ/ITEC/UFPA, Rua Augusto Correa, 01, Belém 66075-110, PA, Brazil

\* Correspondence: darllandorosario@gmail.com

**Abstract:** Non-processed kaolin (flint kaolin) from a mine located in the Capim area (Amazon region, northern Brazil), usually considered as waste, was selected as a source of silicon and aluminum in the synthesis of SAPO-34. This is a molecular sieve and cationic exchanger chosen for tests focusing on the removal of methylene blue in aqueous solutions, which is a cationic dye widely used by textile industries in Brazil. The results revealed that the SAPO-34 has been successfully synthesized with typical cubic morphology, good crystallinity (>90%), and thermal stability (~998 °C). Although the oxidized Fe/Ti impurities contained in the flint kaolin affect the degree of crystallinity of the zeolitic product, its adsorptive properties are not significantly affected, which demonstrates the excellent adsorption results (pH = 11; % removal > 90%). It proved to be an adsorbent with considerable adsorption capacity (9.83 mg·g<sup>-1</sup>). The pH test confirmed the acidic surface characteristics (pH solution 2–4; ↓ removal), and the kinetic model that best fitted the experimental data was pseudo-second-order, with R<sup>2</sup> = 0.998 (kinetics controlled by chemisorption).

**Keywords:** Amazonian kaolin; SAPO-34; separation process; adsorption; dye



**Citation:** Pinheiro, D.R.; Pinheiro, A.P.; Pontes, F.A.; Soares, J.V.K.; Neves, R.F.; Paz, S.P.A. Sapo-34 Obtained from Amazonian Flint Kaolin: Influence of Impurities of “Oxidized Fe/Ti” in Synthesis and Its Application in the Removal of Cationic Dye from Water. *Processes* **2023**, *11*, 662. <https://doi.org/10.3390/pr11030662>

Academic Editors: Monika Wawrzekiewicz and Anna Wołowicz

Received: 19 November 2022

Revised: 22 January 2023

Accepted: 26 January 2023

Published: 22 February 2023



**Copyright:** © 2023 by the authors. Licensee MDPI, Basel, Switzerland. This article is an open access article distributed under the terms and conditions of the Creative Commons Attribution (CC BY) license (<https://creativecommons.org/licenses/by/4.0/>).

## 1. Introduction

The industrial sector has played an important role in the economic and social development of many countries, but environmental problems still often accompany this sector and require solutions. Legislation and inspections for environmental control are becoming tougher (high fines) in most countries around the world. In the case of the dyeing industry, which generates effluents with dyes such as synthetic cationic dyes, there is a problem to be solved. This is because, although they are discharged in diluted form (traces), they still pose risks to the environment and to human beings; due to their stable molecular structures, they usually degrade slowly, making them cumulative over time [1,2].

Different processes (physical, chemical, and biological) for the treatment of these contaminants have been studied, mainly those based on adsorption [3]. Ion exchange-type adsorption has a higher advantage over any process that depends on the degradation of the dyes because, in the process of degradation (photocatalytic, for example), potentially dangerous products can be generated [4,5].

In this context, the ion exchanger-type adsorbent is of great importance, in addition to having the characteristics typically desired for any adsorbent, such as chemical selectivity, thermal stability, and regeneration capacity. Regarding these characteristics, it is possible to highlight zeolites, which have adsorption capacity to ion exchange, physisorption (multilayer adsorption), and chemisorption (monolayer adsorption) [6].

Considering zeolites, we highlight those from the silicoaluminophosphate family, such as SAPO-5, SAPO-11, and SAPO-34. These zeolites are synthetic and have characteristics

that can be adjusted during their synthesis process. The SAPO-34 type attracts attention because it has high thermal and hydrothermal stability and moderate acidity on its surface [7–10]. In general, SAPO-34 is most often obtained from high-purity reagents and is, therefore, expensive. The following precursors are commonly used: silica sol, aerosil, silicon and aluminum silicates, aluminum hydroxide, and/or aluminum isopropoxide. Phosphoric acid is commonly used as a source of phosphorus, and tetraethylammonium hydroxide (TEAOH) and morpholine (MOR) are used as templates or structure-directing agents (SDA) [7,11–13]. The production cost of SAPO-34 is mainly due to the cost of Si and Al reagents, since they are the most frequently consumed. The use of alternative sources of silicon and aluminum in the synthesis of SAPO has been investigated for economic and environmental reasons [14,15].

Note that different research groups in the Amazon have been working with the synthesis of zeolites and/or related structures from beneficiated kaolin, flint kaolin from mine, and kaolin waste [16–21]. The Amazon region leads in the production of kaolin, with the state of Pará responsible for the largest national production, mainly to serve the paper industry. The kaolin product after processing must present certain specifications, such as small particle size and extremely white color [18,22]. Because of this extremely white characteristic, the kaolin extracted from mines for application in the beneficiation process must not present excessive amounts of impurities that reduce the whiteness, since they can make the purification process more expensive. In this context, we highlight flint kaolin. This is a material with the main characteristic being its high particle cohesion and low whiteness due to the presence of iron and titanium oxides, with values that can reach >10%, which make it “sterile” for a noble type of product such as paper coating. This material is temporarily removed from mines to remove the economically viable kaolin for processing, being replaced at the mine itself, which causes a high demand for this material without application [16,17]. The authors indicate that this material, disposed of in a mine, is considered a waste from the process [17,20,21].

In this context, this work aims to evaluate the adsorption of cationic dye (methylene blue) using SAPO-34 synthesized from flint kaolin from the Amazon region. To achieve this, objective SAPO-34 was synthesized by evaluating the influence of the concentration of SDA and impurities present in flint kaolin in the formation of SAPO-34. In relation to cationic dye removal study, the effects of the adsorbent mass, pH, initial concentration of the dye solution, and kinetic study were evaluated considering the adjustment of the pseudo-first order and pseudo-second models.

The work aims to contribute to the synthesis of zeolite SAPO-34 using a raw material with the presence of impurities (Fe/Ti), since the synthesis of SAPO-34 is very sensitive to cationic impurities, which make the process difficult.

## 2. Experimental

### 2.1. Materials

A total of 10 kg of flint kaolin (FK) from the CAPIM mine, located in the Amazon region northeast of the state of Pará, Brazil, was used as a source of Si and Al in the synthesis of SAPO-34.

A thermal pre-treatment of the flint kaolin, which included calcination at 650 °C for 2 h, was performed to obtain flint metakaolin (F-metakaolin). This was then the starting material used together with pure aluminum hydroxide (Synth) which was calcined at 700 °C with phosphoric acid (85%-neon) and morpholine (99%-Synth) as an SDA.

### 2.2. Hydrothermal Synthesis

The synthesis process occurred as follows: in a steel autoclave coated internally with Teflon, the F-metakaolin, distilled water, and calcined aluminum hydroxide were homogenized under magnetic stirring. Subsequently, the following were added: morpholine and phosphoric acid (slowly added). The autoclave was sealed, and the crystallization process occurred in an oven at 200 °C for pre-established lengths of time. After each batch, the

autoclaves were cooled to room temperature, and the supernatant was separated from the sedimented product, which was washed with distilled water under magnetic stirring for 30 min with water changes until pH~7 was reached. Subsequently, the synthesis product was filtered and dried in an air circulation oven for 24 h at 105 °C. The method adopted for the synthesis of SAPO-34 was based on that developed by the International Zeolite Association (IZA) from a sol-gel of  $\text{Al}_2\text{O}_3:1.08\text{SiO}_2:1.06\text{P}:x\text{R}:66\text{H}_2\text{O}$ , where  $x$  is the variation in SDA. In the present study, the SDAs were 0.5, 1, and 2.

The crystallinity (%) was determined by an approximate calculation according to Equation (1):

$$\text{Crystallinity (\%)} = \frac{\sum \text{Peak area}}{\sum \text{Peak area} + \text{baseline area}} \times 100 \quad (1)$$

### 2.3. Effect of Impurities on the Formation of SAPO-34

To evaluate the effects of the impurities contained in flint kaolin, a high-purity kaolin (97.9% in kaolinite) [23] obtained from kaolin processing for paper coating (PK—processed kaolin) was also used.

### 2.4. Characterization of Materials

X-ray diffraction (XRD): A Bruker model D8 ADVANCE X-ray diffractometer with a  $\theta$ - $\theta$  (theta–theta) goniometer and a ceramic X-ray tube with a Cu anode ( $\text{K}\alpha_1$  1.54058 Å) was used. A range of 5 to 75° was used in the analysis. From the XRD data, it was possible to calculate the mean crystallite size of the synthesis products using the Scherer equation [24] (Equation (2)).

$$D = \frac{0.9 \lambda}{\beta \cos \theta} \quad (2)$$

where  $D$  is the crystallite size (nm),  $\lambda$  is the X-ray wavelength (in this case = 1.541874),  $\beta$  is the full width at half maximum (FWHM), and  $\theta$  is the Bragg angle. The mean size of the crystallites was estimated based on planes (101), (110), and (211), and the mean diameter calculated for each sample was used.

Chemical analysis was performed through X-ray fluorescence spectrometry (XRF) using a sequential wavelength dispersive spectroscopy (WDS) instrument, PANalytical model Axios Minerals, with a ceramic X-ray tube, a rhodium (Rh) anode, and a maximum power level of 2.4 KW.

The samples were analyzed using the following preparation: a tablet was pressed with 1 g of the sample + 0.3 g of binder (paraffin wax) on 3 g of substrate (boric acid); this mixture was pressed with a load of 25 tons. Data acquisition and processing were performed using PANalytical's SuperQ Manager software. The loss on ignition (LOI) was determined by burning 1 g of the sample which had been dried at 1000 °C for 1 h.

Thermal Analysis—differential scanning calorimetry, thermogravimetry, and derivative thermogravimetry (DSC-TG-DTG): A NETZSCH STA instrument consisting of a platinum vertical cylinder oven, a digital converter coupled to a microcomputer, a Pt-Rh alloy thermocouple, and an alumina crucible was used as reference. A mass of ~40 mg of the sample was subjected to a temperature sweep from 25 °C to 1100 °C with a heating rate of 10 K/min, under a nitrogen atmosphere.

Scanning electron microscopy (SEM): A Tescan scanning electron microscope (model VEGA3) was used, with an acceleration voltage of 15–20 kV. The samples were deposited on a sample holder with the aid of carbon adhesive tape. The samples were metalized (Au/Pd) to allow the electrical conductivity necessary in the image formation process.

### 2.5. Performance Cationic Dye Adsorption ( $\text{C}_{16}\text{H}_{18}\text{N}_3\text{S}^+$ )

The adsorption proceeded in dynamic conditions with the support of magnetic stirring. After each experimental condition, the samples were collected and centrifuged, and with the aid of a syringe filter, aliquots were collected for analysis by a spectrophotometer.

A stock solution of  $1000 \text{ mg}\cdot\text{L}^{-1}$  methylene blue dye was prepared for use in dye solutions at different concentrations. The following variables were investigated: adsorbent mass (0.1 to 0.5 g); pH (2, 4, 6, 8, 10, and 11), adjusted with NaOH (0.1 M to 1 M); HCl (0.1 M to 1 M) solutions; and initial concentration of dye in the solution (10 to  $30 \text{ mg}\cdot\text{L}^{-1}$ ). The concentrations of the solutions before and after the adsorption tests were determined by UV/VIS spectrophotometry at a wavelength of 664.5 nm (blue).

The dependent variable “amount adsorbed” was calculated by Equation (3), and the adsorption performance was expressed by the removal percentage (Equation (4)).

$$q_t = \frac{(C_i - C_t) \times V}{m} \quad (3)$$

$$\text{removal \%} = \frac{(C_i - C_t)}{C_i} \times 100 \quad (4)$$

where  $C_i$  is the initial concentration of the dye ( $\text{mg}\cdot\text{L}^{-1}$ ),  $C_t$  is the concentration of the solution after a certain time,  $V$  is the volume of the solution (L), and  $m$  is the mass of the adsorbent used (g). The study of the adsorption kinetics was performed by fitting the pseudo-first-order and pseudo-second-order models to the experimental data according to Equations (5) and (6), respectively.

$$q_t = q_e \left(1 - e^{-k_1 t}\right) \quad (5)$$

$$q_t = \frac{t}{\frac{1}{k_2 q_e^2} + \left(\frac{t}{q_e}\right)} \quad (6)$$

where  $q_e$  and  $q_t$  are the sorption capacities at equilibrium and as a function of time, respectively ( $\text{mg}\cdot\text{g}^{-1}$ );  $k_1$  is the sorption constant of the pseudo-first-order model ( $\text{min}^{-1}$ ); and  $k_2$  is the sorption constant of the pseudo-second-order model ( $\text{g}\cdot\text{mg}^{-1}\cdot\text{min}^{-1}$ ).

### 3. Results and Discussion

#### 3.1. Characterization of the Flint Kaolin

Figure 1 shows the X-ray diffractogram of the flint kaolin (FK). It can be observed that the material is composed mainly of clay mineral kaolinite ( $d_{001} = 7.12 \text{ \AA}$ ), according to the ICDD standard 01-083-0971, with the presence of hematite minerals ( $d_{110} = 3.68 \text{ \AA}$ ) and anatase ( $d_{101} = 3.52 \text{ \AA}$ ) indexed by ICDD 01-073-0603 and ICDD 00-021-1272, respectively. However, in the diffractogram of the processed kaolin (PK), only peaks related to kaolinite are identified, and peaks of anatase and hematite are not identified because they were below the limit of XRD detection (<1%).

When comparing the two diffractograms (Figure 1), there is a difference in the degree of stacking disorder between the kaolinite of the flint kaolin (FK, non-processed kaolin) and that of the processed kaolin (PK) (see highlighted area in Figure 1, region  $19\text{--}24^\circ 2\theta \text{ \AA Cu}$ ). When presenting a triplet, the PK kaolinite has fewer defects in the crystalline structure than the FK kaolinite, which has a singlet. More defects or less crystallinity indicates higher reactivity [17].

The chemical composition of the flint kaolin is shown in Table 1.  $\text{SiO}_2$  and  $\text{Al}_2\text{O}_3$  are the main constituents because they are related to kaolinite.  $\text{TiO}_2$  and  $\text{Fe}_2\text{O}_3$  are related to the minerals anatase and hematite, which are typical of kaolin from this region [16–18]. The chemical composition of flint kaolinite corroborates the mineralogical characterization observed in the diffractogram of Figure 1.

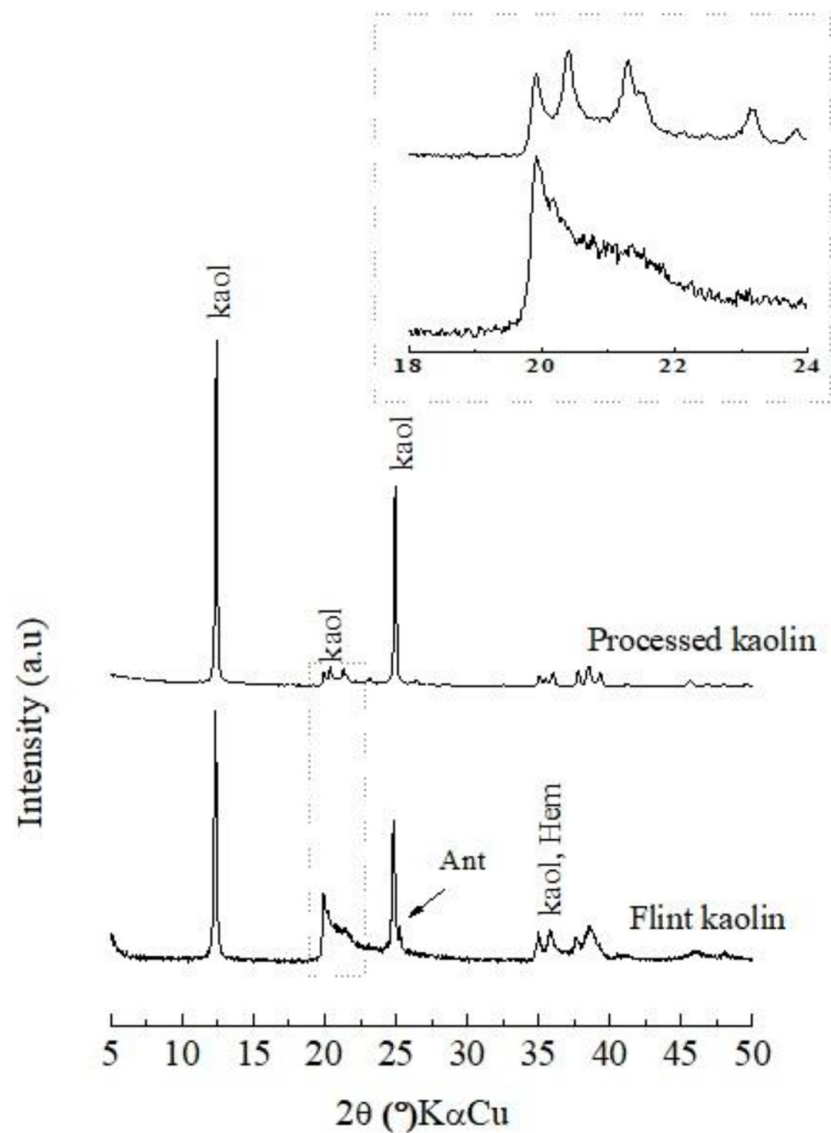


**Figure 1.** XRD flint kaolin and processed kaolin: kaol = kaolinite; Ant = anatase; Hem = hematite.

**Table 1.** Chemical composition of the flint kaolin.

Components (%)	Flint Kaolin
SiO <sub>2</sub>	42.85
Al <sub>2</sub> O <sub>3</sub>	36.78
Fe <sub>2</sub> O <sub>3</sub>	2.75
TiO <sub>2</sub>	3.05
LOI (loss on ignition)	14.15

### 3.2. Effect of SDA and Time on Crystallinity

Figures 2–4 show the effect of the SDA and time on the formation and crystallinity of the CHA structure. For a time of 5 h and considering all molar ratios ( $x = 0.5$ ,  $x = 1$ ,  $x = 2$ ), ALPO (ICDD 00-051-1674) and tridymite (ICDD 01-083-2299) phases were formed.

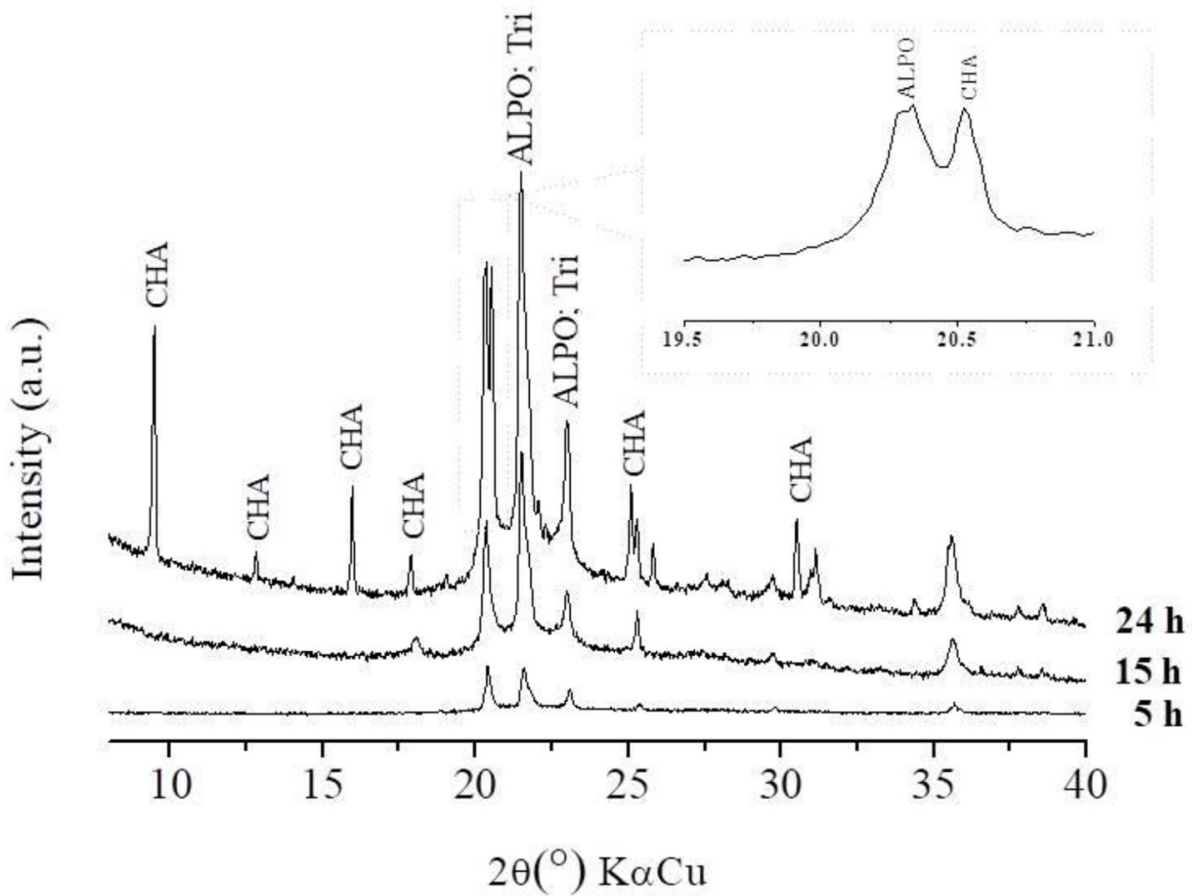


**Figure 2.**  $x = 0.5$ ; crystallization time = 5, 15, and 24 h.

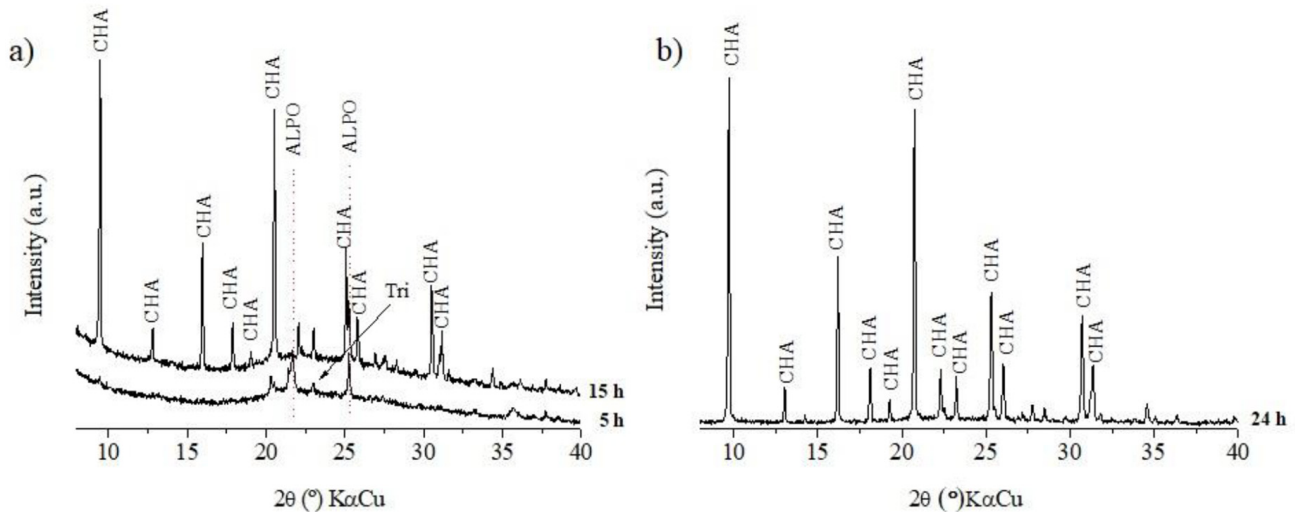


**Figure 3.**  $x = 1$ : (a) crystallization time = 5 and 15 h; (b) crystallization time = 24 h.

As time progressed (Figure 2), for  $x = 0.5$ , silicon ions were also incorporated into the ALPO phase structure, which made the peaks associated with the CHA structure—characteristic of SAPO-34—more evident. However, the availability of SDA was low, which could possibly result in the incomplete binding of the silicon ions; they can be identified in the diffractogram (Figure 2) through characteristic peaks as tridymite ( $SiO_2$ ), even for the maximum duration of synthesis (24 h) [25–28].

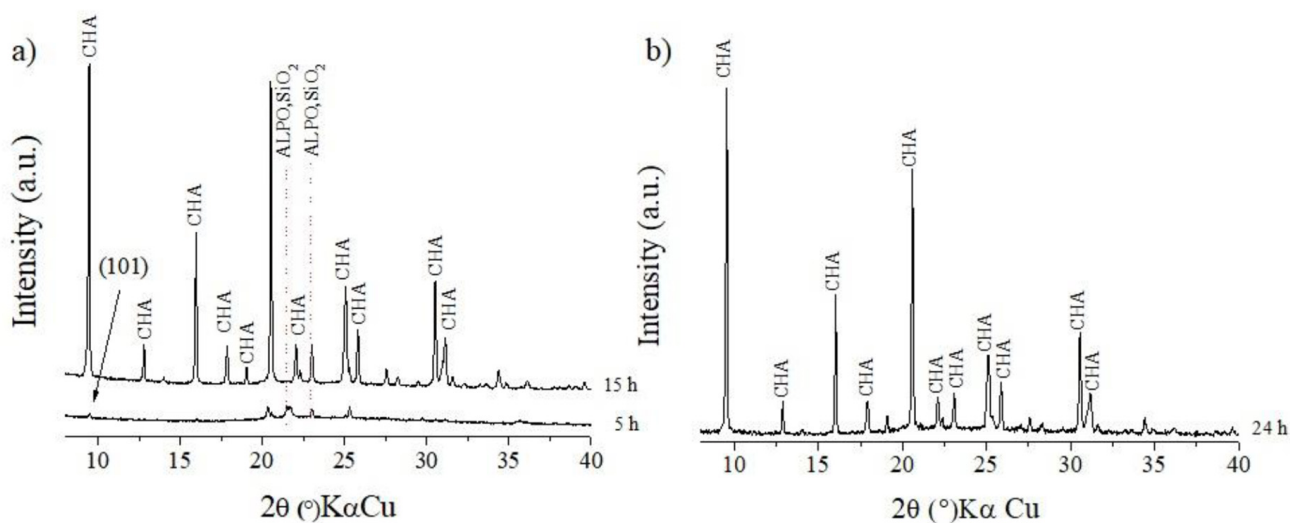


**Figure 4.**  $x = 2$ : (a) crystallization time = 5 and 15 h; (b) crystallization time = 24 h.

In contrast, for  $x = 1$  and  $x = 2$  (Figures 3 and 4), the increase in the amount of morpholine significantly increased the formation of the CHA structure in a shorter amount of time, whereas the peaks of tridymite evidenced for  $x = 0.5$  were absent at 15 h ( $x = 1$  and  $x = 2$ ). This observation is related to the positive effect of SDA on the SM2 and SM3 substitution mechanisms. Studies show that an increase in SDA in the synthesis promotes favorable conditions not only with the function of directing the structure, but also with importance in the distribution of silicon in the structure [29–32].

According to the results and the literature [7,14,33], the synthesis using F-metakaolin followed the crystallization mechanism for silicoaluminophosphates. A possible crystallization mechanism as a function of the amount of SDA and time using flint metakaolin is briefly described as follows:

- i The Si-O and Al-O of the F-metakaolinite are hydrolyzed and transferred by diffusion from the solid to the medium at different rates. The aluminum ions have a tendency to form secondary building units (SBUs) of 6-membered rings with phosphorus and hydroxyl ions, indicating that Al-O is transferred faster than Si-O, which affects the preliminary formation ( $t = 5$  h) of the ALPO phase in the entire XRD pattern [14,33].
- ii Under hydrothermal conditions for  $x = 0.5, 1,$  and  $2$ , primary building units (PBUs) are formed with subsequent formation of secondary building units (SBUs). As time progresses, the amount of PBUs decreases, the amount of SBUs increases, and a saturation stage is achieved where nucleation begins [33]. An increase in the amount of SDA may affect the mechanism of formation of these building units, since for  $x = 2$  and a time of 5 h, a small peak in  $d_{101}$  (Figure 5) for SAPO-34 is observed. This indicates that the SDA may affect the incorporation of silicon ions already in the building units, which affects the formation of nuclei and the growth of SAPO-34 crystals in a shorter time. The XRD pattern for the sample,  $x = 0.5$ , for example, indicates that the nuclei begin to grow without silicon ions in the structure, and as time progresses, the increase in the Si-O concentration in the medium causes the Si ions to begin to be incorporated into the structure of the crystals formed by ALPO.

The SDA accelerated the substitution mechanisms, promoting an increase in the SAPO-34 phase and a consequent increase in the crystallinity (Figure 5) of the products obtained as a function of time, which favored the growth rate of the crystals [18–20].

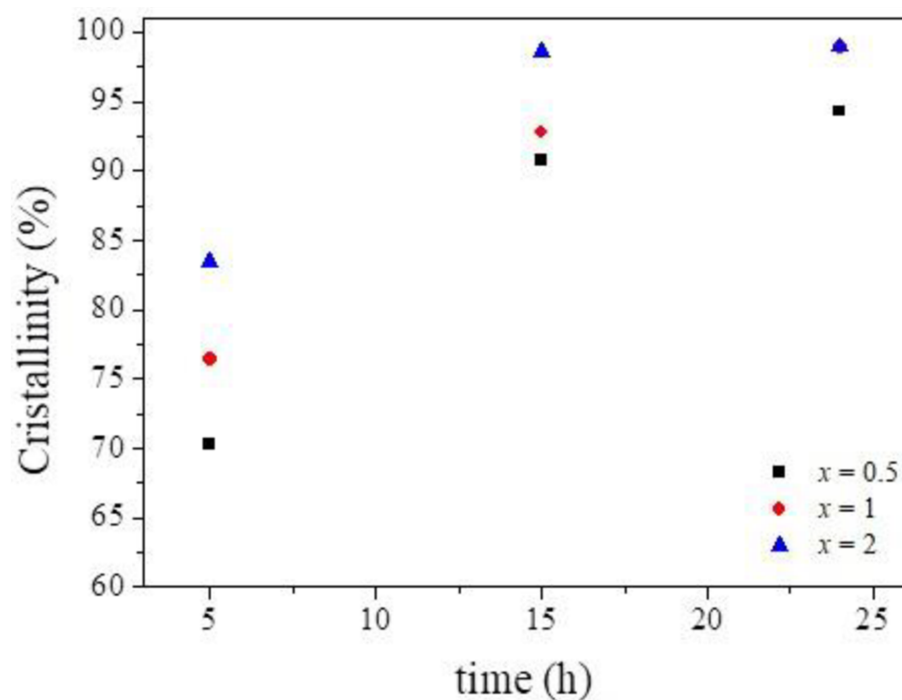


**Figure 5.** Crystallinity curve.

The crystallinity values reached approximately 98.5% and 99% in 24 h for  $x = 1$  and  $x = 2$ , respectively. Increasing the ratio to  $x = 1$  and  $x = 2$  relative to  $x = 0.5$  promoted an increase in the crystallinity and a decrease in undesired phases, such as the ALPO and tridymite phases. This behavior was also observed in previous studies, which related the increase of the SDA amount to the formation of the CHA structure in less time and without the presence of phases considered impurities [18–20]. However, for this study, we considered the ratio of SDA to be  $x = 1$ , synthesized at 24 h for use in adsorption, for economic reasons. Once these optimized conditions for obtaining SAPO-34 from flin metakaolinite were selected, i.e.,  $x = 1$  and 24 h of crystallization, we performed a detailed characterization.

Figure 6 shows the TG, DTG, and DSC curves of the sample ( $x = 1$  and 24 h of crystallization). Three thermal weight loss events stand out, which we identified as I, II, and III. The first weight loss (I) was related to the physical water desorption from the sample, which occurred in the temperature range from 25 °C to 200 °C and agreed with the endothermic peak present in the DSC curve. Thermal event II was the region of greatest weight loss, which occurred between 200 and 500 °C and was related to the decomposition of morpholine, which was used as an SDA. The intense and accentuated peak was related to this thermal transformation, which involved high energy, since there was a strong interaction between SDA and the SAPO-34 structure. The third weight loss (III), above 500 °C, was related to the volatilization of the waste from the combustion of morpholine in the SAPO-34 channels [28,34]. Because events II and III were related to the decomposition of morpholine by combustion, they released energy, which is evidenced in the DSC curve by the exothermic peaks. The exothermic peak at ~998 °C is related to the collapse of the molecular sieve structure, thus indicating good thermal stability.

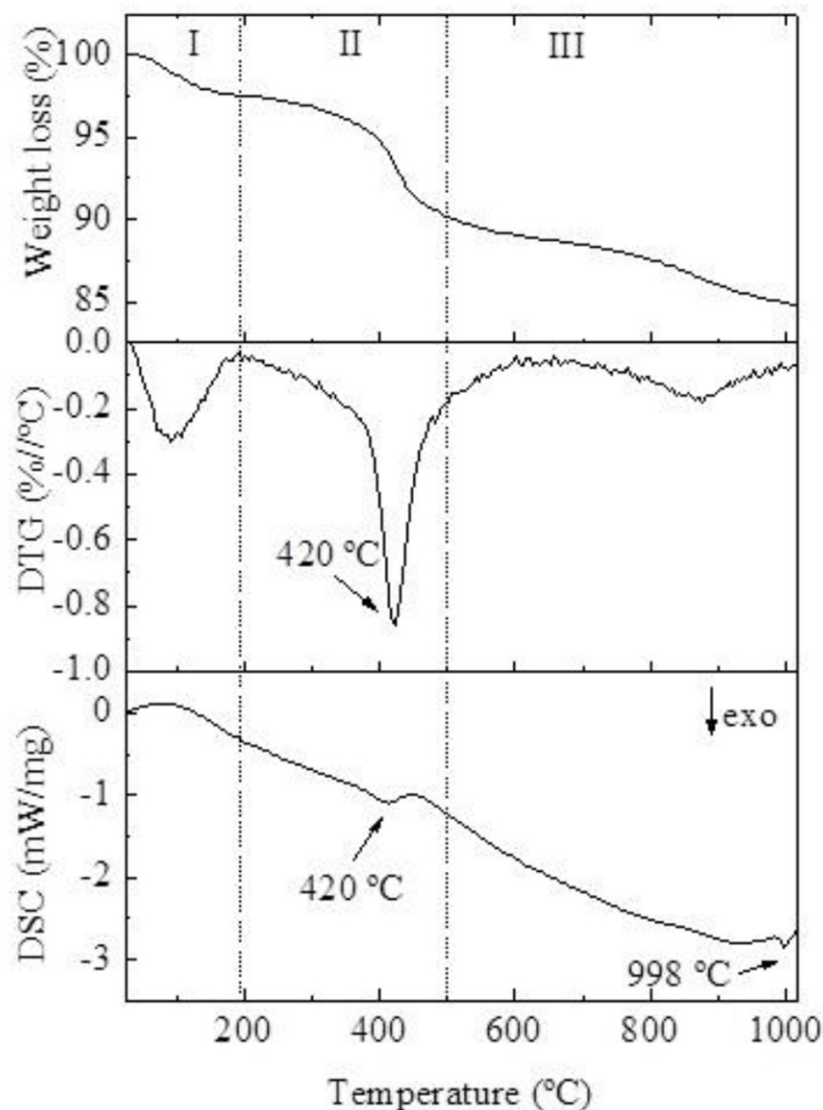


**Figure 6.** TG, DTG, and DSC curves of the sample.

### 3.3. Effects of Oxidized Fe and Ti on the Formation of SAPO-34

A study was performed to compare the SAPO-34 obtained from the F-metakaolin (S-FMK) to that obtained from the P-metakaolin (S-PMK), 97.9%, in kaolinite, to evaluate the interference of Fe and Ti ion impurities on the formation of this type of zeolite. Figure 7a shows the X-ray diffractograms of these products, and in both, the CHA phase is present. However, when we analyzed the main peak ( $d_{101} = 9.254$ ) of the product synthesized with F-metakaolin, we noticed a small displacement of the peak to a lower angle. The intense peak for the standard sample is at position  $2\theta = 9.6$  ( $K\alpha Cu$ ) ( $d = 9.167$  Å), while the F-metakaolin product has a more intense peak at position  $2\theta = 9.5^\circ$  ( $K\alpha Cu$ ) ( $d = 9.254$  Å), which indicates a slight increase in interplanar distance. In the first analysis, flint kaolin had 3.05% titanium oxide plus 2.75% iron oxide; these metal ions (Fe or Ti ions) may have been incorporated in the structure of the product obtained, or the tetrahedral already containing Fe and Ti from the flint kaolin could have been rearranged in the structure of the synthesized product. Considering that titanium and iron have ionic radii greater than those of silicon and aluminum, this incorporation generates an elongation in the Ti-O or Fe-O bonds compared to the Si-O or Al-O bonds.

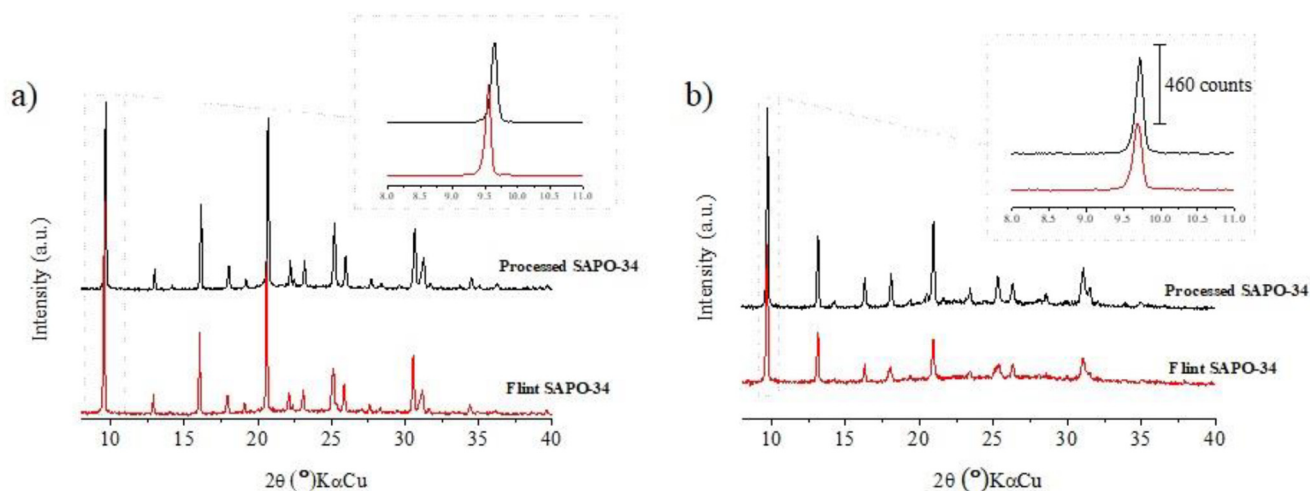


**Figure 7.** (a) Comparison of the products synthesized: XRD processed SAPO-34 (non-calcined) and flint SAPO-34 (non-calcined); (b) XRD processed SAPO-34 (calcined) and flint SAPO-34 (calcined).

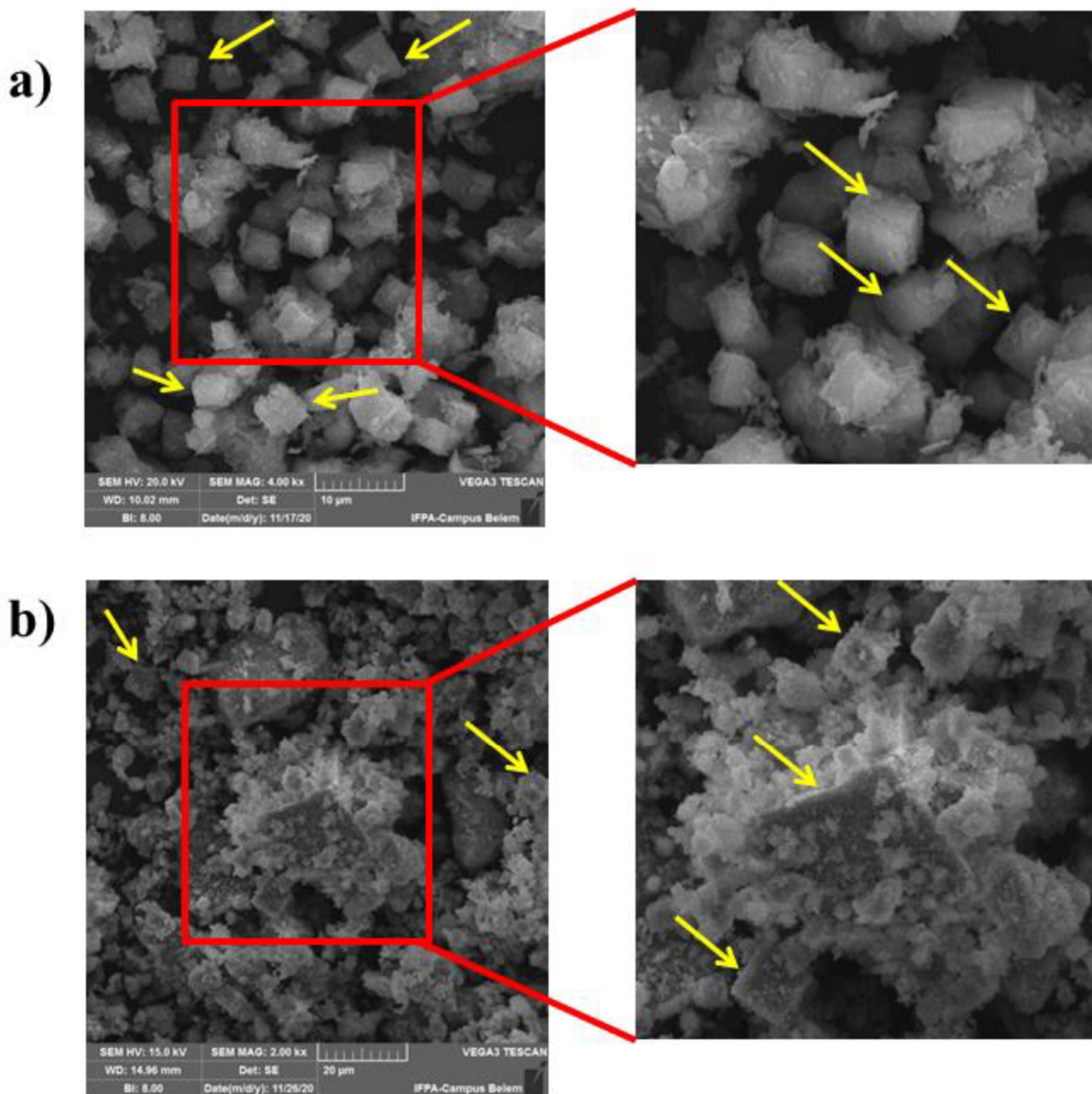
Figure 7b shows the diffractograms of the calcined products (S-PMK-Calcined and S-FMK-Calcined). It can be observed that the sample from the F-metakaolin had a more pronounced decrease in peak intensity than the standard sample. It can also be observed that for the peak of higher intensity (Figure 7b), the previously reported displacement did not occur, indicating that the SDA affected the structure before calcination, causing a small change in the interplanar distance. This did not occur when the samples were calcined [28,35–37].

The mean diameter value of the calcined sample was 79.7 nm for the standard sample and 69.1 nm the sample synthesized with F-metakaolin. The decrease in crystallite size may be related to the decrease in the intensity (Figure 7b) of the sample with F-metakaolin compared to the calcined XRD pattern, which may be related to the presence of titanium and iron ions from the flint kaolin. These ions are considered to be impurities that can interfere with the growth of crystallites. The isomorphic substitution (of Al ions by Fe ions) that occurs for kaolinite from FK can also occur during the formation of the molecular sieve, which causes an expansion of the unit cell size and a consequent reduction in the crystallinity [36].

Figure 8 shows SEM micrographs for the calcined samples: S-PMK-Calcined (Figure 8a) and S-FMK-Calcined (Figure 8b). The samples have characteristic cubic morphologies for SAPO-34 (yellow arrows). However, for the sample synthesized with the flint kaolin, it can be observed that many scraps are agglomerated on the surface of the cubic crystals, showing a possible influence of the impurities present (Fe and Ti ions) in the flint kaolin.

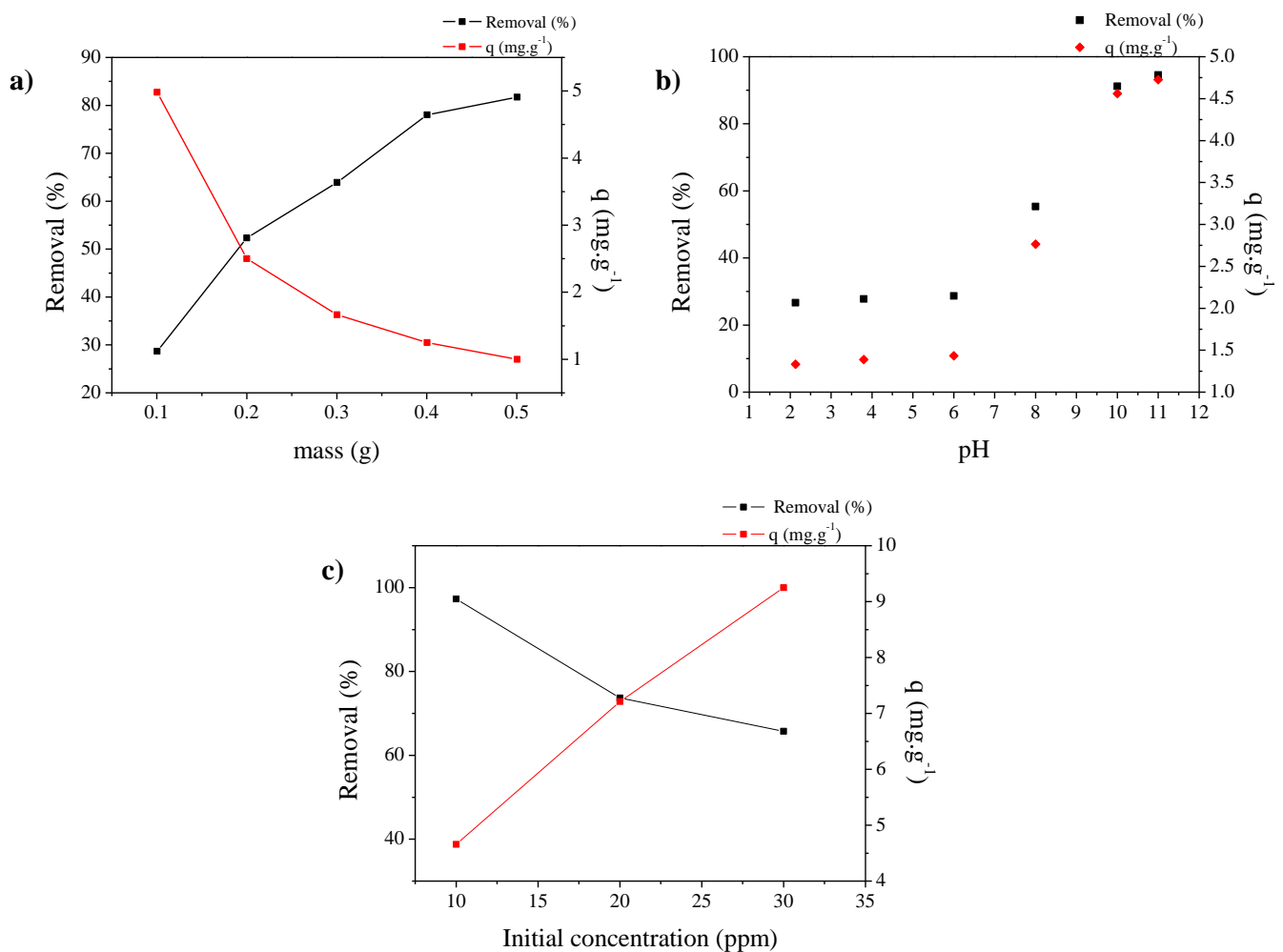
### 3.4. Study of Cationic Dye Adsorption ( $C_{16}H_{18}N_3S^+$ )

Figure 9 shows results of dye adsorption. Figure 9a shows a summary of the responses “Removal %” and “Adsorbed Amount” to verify the performance as a function of the adsorbent mass. An increase in the adsorbent mass increases the dye removal. Thus, methylene blue removal from SAPO-34 is relevant because it reached values of ~81.7%. In turn, when the adsorbed amount (adsorption capacity) is evaluated as a function of mass, a decrease in these values can be observed. This decrease with the increasing mass can be explained by the agglomeration of the zeolite particles due to the increase in mass, which consequently decreases the availability of active sites [38–40]. Thus, the amount of adsorbent considered optimal for the other study variables is 0.1 g, which provides the highest adsorption capacity—approximately  $5 \text{ mg} \cdot \text{g}^{-1}$  of adsorbent.



**Figure 8.** SEM: (a) processed SAPO-34-Calcined and (b) flint SAPO-34-Calcined.

Figure 9b shows the effect of pH on the ability to remove and adsorb a solution with an initial dye concentration of  $10 \text{ mg}\cdot\text{L}^{-1}$ . It can be observed that there was an increase in the removal and adsorption capacity when the pH value increased, reaching maximum values at a pH equal to 11. Figure 9b shows the effect of pH on the removal capacity ( $\text{mg}\cdot\text{g}^{-1}$ ) from a solution with an initial dye concentration of  $10 \text{ mg}\cdot\text{L}^{-1}$ . It can be observed that there was an increase in the removal capacity when the pH value increased, reaching maximum values at a pH equal to 11. This behavior can be explained by the acidic characteristics (active site) of the SAPO-34 adsorbent, which reached a low pH value (pH region between 2 to 4) where protonation of the adsorbent surface occurred. In acidic solution, there was an excess of  $\text{H}_3\text{O}^+$  with the presence of  $\text{C}_{16}\text{H}_{18}\text{N}_3\text{S}^+$  of the dye; thus, there was competition between the cationic part of the dye ( $\text{C}_{16}\text{H}_{18}\text{N}_3\text{S}^+$ ) and the  $\text{H}_3\text{O}^+$  ions with the surface by electrostatic repulsion [41]. In turn, when the pH of the solution was raised above this range (pH 6 to 11), the surface of the adsorbent tended to become negatively charged, resulting in a reduction in  $\text{H}_3\text{O}^+$  ions in the solution, thus favoring the adsorption of  $\text{C}_{16}\text{H}_{18}\text{N}_3\text{S}^+$  [38,39].



**Figure 9.** (a) Effect of mass on removal % and adsorption capacity; (b) effect of pH on removal % and adsorption capacity; (c) effect of the initial concentration.

Figure 9c shows the effect of the initial concentration of dye, considering the pH to be 11 and the adsorbent mass to be 0.1 g. The behavior of the adsorption capacity was practically linear with increasing initial concentration, and this growth was expected because when the initial concentration increased, the concentration gradient increased, thus favoring higher adsorption; however, there was a decrease in the removal due to the availability of sites, which reduced the removal capacity [38–40].

Figure 10a,b show the adsorption kinetics and the fitting of the experimental data to the kinetic models, respectively (pseudo-first-order and pseudo-second-order), considering an initial concentration of  $10 \text{ mg}\cdot\text{L}^{-1}$ , room temperature, adsorbent mass of 0.1 g, and pH 11.

From the coefficient of determination data (Table 2), the pseudo-second-order model best fit the experimental data, because the value of this parameter was the closest to the unit and the RMSE data were low compared to those obtained for the pseudo-first-order model. This model assumes that the adsorption rate is controlled by chemisorption involving valence forces (electrostatic) [38–40,42].

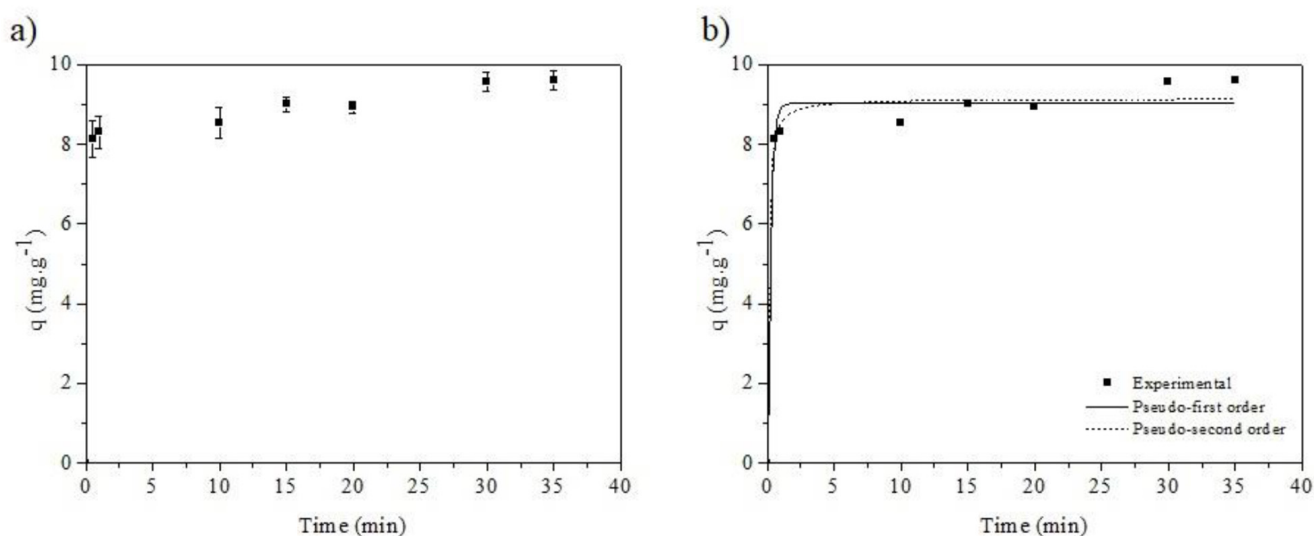


Figure 10. Pseudo-first-order kinetic model and pseudo-second-order kinetic model.

Table 2. Parameters of the kinetic models fitted to the experimental data.

Pseudo-First-Order				Pseudo-Second-Order			
$k_1$ ( $\text{min}^{-1}$ )	$q_e$ ( $\text{mg}\cdot\text{g}^{-1}$ )	$R^2$	RMSE	$k_2$ ( $\text{g}\cdot\text{mg}^{-1}\cdot\text{min}^{-1}$ )	$q_e$ ( $\text{mg}\cdot\text{g}^{-1}$ )	$R^2$	RMSE
4.32	9.03	0.97	0.46	1.48	9.15	0.99	0.47

#### 4. Conclusions

In summary, flint kaolin was used successfully as a low-cost alternative for the synthesis of SAPO-34. The results show that the amount of SDA affected the crystallization mechanism for the formation of the molecular sieve. XRD, DSC-TG-DTG, and SEM analysis confirmed that the synthesized SAPO-34 presented good crystallinity which was affected possibly by Ti and Fe impurities; excellent thermal stability, with collapse of the structure at a temperature above 900 °C; and typical cubic morphology. From the point of view of sorption, through the tests performed, the material that showed the best crystallinity (>90%) with the lowest amount of SDA proved to be an option for the removal of the methylene blue dye.

Moreover, the effect of the pH (2–4 ↓ removal; pH = 11 ↑ removal) on adsorption showed the acidic characteristics of the formed material. The adsorption mechanism of the system adsorbent–adsorbate is compatible with pseudo-second-order kinetics (kinetics controlled by chemisorption). Finally, this research aimed to contribute to the literature by demonstrating alternative raw materials for the synthesis of SAPO-34.

The research presents an opportunity to apply this zeolite synthesized from Amazon mining tailings in adsorption processes. Future works will be carried out in addition to this preliminary one, aiming at more careful analyses for the evaluation of the adsorption process (FTIR, SEM, zeta potential, study of isotherms, and thermodynamic study). For the synthesis process, through DOE, we optimized the synthesis to make it more environmentally friendly, with a greater reduction in SDA and phosphoric acid.

**Author Contributions:** Conceptualization, D.R.P., A.P.P., F.A.P., J.V.K.S., R.F.N. and S.P.A.P.; methodology, D.R.P.; validation, D.R.P., A.P.P., F.A.P., J.V.K.S., R.F.N. and S.P.A.P.; formal analysis, D.R.P. and S.P.A.P.; investigation, D.R.P., A.P.P., F.A.P., J.V.K.S., R.F.N. and S.P.A.P.; resources, D.R.P., A.P.P. and S.P.A.P.; writing—original draft preparation, D.R.P.; writing—review and editing, D.R.P. and S.P.A.P.; supervision, S.P.A.P.; funding acquisition, D.R.P. and S.P.A.P. All authors have read and agreed to the published version of the manuscript.

**Funding:** Conselho Nacional de Desenvolvimento Científico e 377 Tecnológico-CNPq (process No.: 141491/2017-5). This study was also financed in part by the Coordenação de Aperfeiçoamento de Pessoal de Nível Superior—Brasil (CAPES)-Finance Code 001.

**Acknowledgments:** The authors dedicate this paper to the memory of Nielson Fernando da Paixão Ribeiro, who sadly passed away on Sunday 23 August 2020. We express our gratitude to the great professional, researcher, friend, and colleague who was Nielson. The authors thank the Brazilian agency CNPq (Conselho Nacional de Desenvolvimento Científico e Tecnológico) for the doctoral scholarship to the first author (process No.: 141491/2017-5). This study was also financed in part by the Coordenação de Aperfeiçoamento de Pessoal de Nível Superior—Brasil (CAPES)-Finance Code 001. We also thank the Pró-Reitoria de Pesquisa e Pós-Graduação—Universidade Federal do Pará (PROPESP/UFPA) for funding support (EDITAL PAPQ No. 01/2020). We also thank the Graduate Program in Physics of UFPA (PPGF/UFPA) and the Graduate Program in Geology and Geochemistry of UFPA (PPGG/UFPA) for the use of its laboratories.

**Conflicts of Interest:** The authors declare no conflict of interest.

## References

1. Holkar, C.R.; Jadhav, A.J.; Pinjari, D.V.; Mahamuni, N.M.; Pandit, A.B. A critical review on textile wastewater treatments: Possible approaches. *J. Environ. Manag.* **2016**, *182*, 351–366. [[CrossRef](#)]
2. Mittal, H.; Babu, R.; Dabbawala, A.A.; Stephen, S.; Alhassan, S.M. Zeolite-Y incorporated karaya gum hydrogel composites for highly effective removal of cationic dyes. *Colloids Surf. A Physicochem. Eng. Asp.* **2020**, *586*, 124161. [[CrossRef](#)]
3. Wu, J.-S.; Liu, C.-H.; Chu, K.H.; Suen, S.-Y. Removal of cationic dye methyl violet 2B from water by cation exchange membranes. *J. Membr. Sci.* **2008**, *309*, 239–245. [[CrossRef](#)]
4. Joseph, J.; Radhakrishnan, R.C.; Johnson, J.K.; Joy, S.P.; Thomas, J. Ion-exchange mediated removal of cationic dye-stuffs from water using ammonium phosphomolybdate. *Mater. Chem. Phys.* **2020**, *242*, 122488. [[CrossRef](#)]
5. Karcher, S.; Kornmuller, A.; Jekel, M. Anion exchange resins for removal of reactive dyes from textile wastewaters. *Water Res.* **2002**, *36*, 4717–4724. [[CrossRef](#)]
6. Aljerf, L. High-efficiency extraction of bromocresol purple dye and heavy metals as chromium from industrial effluent by adsorption onto a modified surface of zeolite: Kinetics and equilibrium study. *J. Environ. Manag.* **2018**, *225*, 120–132. [[CrossRef](#)]
7. Sun, Q.; Xie, Z.; Yu, J. The state-of-the-art synthetic strategies for SAPO-34 zeolite catalysts in methanol-to-olefin conversion. *Natl. Sci. Rev.* **2018**, *5*, 542–558. [[CrossRef](#)]
8. Jhung, S.H.; Chang, J.-S.; Hwang, J.S.; Park, S.-E. Selective formation of SAPO-5 and SAPO-34 molecular sieves with microwave irradiation and hydrothermal heating. *Microporous Mesoporous Mater.* **2003**, *64*, 33–39. [[CrossRef](#)]
9. Askari, S.; Sedighi, Z.; Halladj, R. Rapid synthesis of SAPO-34 nanocatalyst by dry gel conversion method templated with morpholine: Investigating the effects of experimental parameters. *Microporous Mesoporous Mater.* **2014**, *197*, 229–236. [[CrossRef](#)]
10. Askari, S.; Bashardoust Siahmard, A.; Halladj, R.; Miari Alipour, S. Different techniques and their effective parameters in nano SAPO-34 synthesis: A review. *Powder Technol.* **2016**, *301*, 268–287. [[CrossRef](#)]
11. Wang, T.; Lu, X.; Yan, Y. Synthesis, characterization and crystallization mechanism of SAPOs from natural kaolin. *Microporous Mesoporous Mater.* **2010**, *136*, 138–147. [[CrossRef](#)]
12. Wang, Q.; Wang, L.; Wang, H.; Li, Z.; Wu, H.; Zhang, X.; Zhang, S. Synthesis, characterization and catalytic performance of SAPO-34 molecular sieves for methanol-to-olefin (MTO) reaction. *Asia-Pac. J. Chem. Eng.* **2011**, *6*, 596–605. [[CrossRef](#)]
13. Xing, A.; Yuan, D.; Tian, D.; Sun, Q. Controlling acidity and external surface morphology of SAPO-34 and its improved performance for methanol to olefins reaction. *Microporous Mesoporous Mater.* **2019**, *288*, 109562. [[CrossRef](#)]
14. Wang, T.; Lu, X.; Yan, Y. Synthesis of SAPO-34 from metakaolin: Crystallization mechanism of SAPO-34 and transformation process of metakaolin. *Microporous Mesoporous Mater.* **2013**, *168*, 155–163. [[CrossRef](#)]
15. Pinheiro, D.R.; Gonçalves, L.R.; Sena, R.L.P.; Martelli, M.C.; Neves, R.F.; Ribeiro, N.F.P. Industrial Kaolin Waste as Raw Material in the Synthesis of the SAPO-34 Molecular Sieve. *Mater. Res.* **2020**, *23*, e20200043. [[CrossRef](#)]
16. Carneiro, B.S.; Angélica, R.S.; Sheller, T.; Castro, E.A.S.; Neves, R.F. Caracterização de fase do caulim duro da região do Rio Capim, Pará. *Cerâmica* **2003**, *49*, 237–244. [[CrossRef](#)]
17. Rocha Junior, C.A.F.; Angélica, R.S.; Neves, R.F. Síntese de zeólita do tipo faujasita: Comparação entre caulim beneficiado e caulim flint. *Rev. Cerâmica* **2015**, *61*, 259–268. [[CrossRef](#)]
18. Menezes, R.A.; Paz, S.P.A.; Angélica, R.S.; Neves, R.F.; Neumann, R.; Faulstich, F.R.L.; Pergher, S.B.C. Synthesis of ultramarine pigments from Na-A zeolite derived from kaolin waste from the Amazon. *Clay Miner.* **2017**, *52*, 83–95. [[CrossRef](#)]
19. Castro, P.R.S.; Maia, A.A.B.; Angélica, R.S. Study of the Thermal Stability of Faujasite Zeolite Synthesized from Kaolin Waste from the Amazon. *Mater. Res.* **2019**, *22*, e20190321. [[CrossRef](#)]
20. De Nazaré de Oliveira, A.; Tallyta Leite Lima, E.; de Aguiar Andrade, E.H.; Zamian, J.R.; Filho da Rocha, G.N.; da Costa Ferreira, C.E.; de Oliveira Pires, L.H.; Luque, R.; Santos dos Nascimento, L.A. Acetylation of Eugenol on Functionalized Mesoporous Aluminosilicates Synthesized from Amazonian Flint Kaolin. *Catalysts* **2020**, *10*, 478. [[CrossRef](#)]

21. De Nazaré de Oliveira, A.; de Oliveira, D.T.; Angélica, R.S.; Andrade de Aguiar, E.H.; do Rosario da Silva, J.K.; da Rocha Filho, G.N.; Coral, N.; de Oliveira Pires, L.H.; Santos dos Nascimento, L.A. Efficient esterification of eugenol using a microwave-activated waste kaolin. *React. Kinet. Mech. Catal.* **2020**, *130*, 633–653. [[CrossRef](#)]
22. Menezes, R.A.; Aranha da Paz, S.P.; Angélica, R.S.; Neves, R.F.; Castella Pergher, S.B. Color and shade parameters of ultramarine zeolitic pigments synthesized from kaolin waste. *Mater. Res.* **2014**, *17* (Suppl. S1), 23–27. [[CrossRef](#)]
23. Aranha da Paz, S.P.; Angélica, R.S.; Kahn, H. Optimization of the reactive silica quantification method applied to Paragominas-type gibbsitic bauxite. *Int. J. Miner. Process.* **2017**, *162*, 48–57. [[CrossRef](#)]
24. Akhgar, S.; Towfighi, J.; Hamidzadeh, M. Investigation of synthesis time and type of seed along with reduction of template consumption in the preparation of SAPO-34 catalyst and its performance in the MTO reaction. *RSC Adv.* **2020**, *10*, 34474–34485. [[CrossRef](#)]
25. Prakash, A.M.; Unnikrishnan, S. Synthesis of SAPO-34: High Silicon Incorporation in the Presence of Morpholine as Template. *J. Chem. Soc. Faraday Trans.* **1994**, *90*, 2291–2296. [[CrossRef](#)]
26. Vomscheid, R.; Briend, M.; Peltre, M.J.; Man, P.P.; Barthomeuf, D. The Role of the Template in Directing the Si Distribution in SAPO Zeolites. *J. Phys. Chem.* **1994**, *98*, 9614–9618. [[CrossRef](#)]
27. Tan, J.; Liu, Z.; Bao, X.; Liu, X.; Han, X.; He, C.; Zhai, R. Crystallization and Si incorporation mechanisms of SAPO-34. *Microporous Mesoporous Mater.* **2002**, *53*, 97–108. [[CrossRef](#)]
28. Doan, T.; Nguyen, K.; Dam, P.; Vuong, T.H.; Le, M.T.; Thanh, H.P. Synthesis of SAPO-34 Using Different Combinations of Organic Structure-Directing Agents. *J. Chem.* **2019**, *2019*, 6197527. [[CrossRef](#)]
29. Muñoz, T.A.; Márquez, C.; Sastre, E. Use of different templates on SAPO-34 synthesis: Effect on the acidity and catalytic activity in the MTO reaction. *Catal. Today* **2012**, *179*, 27–34. [[CrossRef](#)]
30. Li, G.; Wang, B.; Sun, Q.; Xu, W.Q.; Ma, Z.; Wang, H.; Zhang, D.; Zhou, J. Novel synthesis of fly-ash-derived Cu-loaded SAPO-34 catalysts and their use in selective catalytic reduction of NO with NH<sub>3</sub>. *Green Energy Environ.* **2019**, *4*, 470–482. [[CrossRef](#)]
31. Li, M.; Wang, Y.; Bai, L.; Chang, N.; Nan, G.; Hu, D.; Zhang, Y.; Wei, W. Solvent-free synthesis of SAPO-34 nanocrystals with reduced template consumption for methanol-to-olefins process. *Appl. Catal. A Gen.* **2017**, *531*, 203–211. [[CrossRef](#)]
32. Liu, H.; Kianfar, E. Investigation the Synthesis of Nano-SAPO-34 Catalyst Prepared by Different Templates for MTO Process. *Catal. Lett.* **2020**, *151*, 787–802. [[CrossRef](#)]
33. Luo, M.; Liu, M.; Fu, Y.; Chen, W.; Wang, B.; Mao, G. TEOH-Templated SAPO-34 Zeolite with Different Crystallization Processes and Silicon Sources: Crystallization Mechanism and MTO Performance. *Eur. J. Inorg. Chem.* **2020**, *2020*, 318–326. [[CrossRef](#)]
34. Herrero, I.P.; Álvarez, C.M.; Sastre, E. Complex relationship between SAPO framework topology, content and distribution of Si and catalytic behaviour in the MTO reaction. *Catal. Sci. Technol.* **2017**, *7*, 3892–3901. [[CrossRef](#)]
35. Zhang, D.; Wei, Y.; Xu, L.; Chang, F.; Liu, Z.; Meng, S.; Su, B.L.; Liu, Z. MgAPO-34 molecular sieves with various Mg stoichiometries: Synthesis, characterization and catalytic behavior in the direct transformation of chloromethane into light olefins. *Microporous Mesoporous Mater.* **2008**, *116*, 684–692. [[CrossRef](#)]
36. Andonova, S.; Tamm, S.; Montreuil, C.; Lambert, C.; Olsson, L. The effect of iron loading and hydrothermal aging on one-pot synthesized Fe/SAPO-34 for ammonia SCR. *Appl. Catal. B Environ.* **2016**, *180*, 775–787. [[CrossRef](#)]
37. Mazur, M.; Kasneryk, V.; Přeč, J.; Brivio, F.; Hernández, C.O.; Mayoral, A.; Kubů, M.; Čejka, J. Zeolite framework functionalisation by tuneable incorporation of various metals into the IPC-2 zeolite. *Inorg. Chem. Front.* **2018**, *5*, 2746–2755. [[CrossRef](#)]
38. Ghahremani, R.; Baheri, B.; Peydayesh, M.; Asarehpour, S.; Mohammadi, T. Novel crosslinked and zeolite-filled polyvinyl alcohol membrane adsorbents for dye removal. *Res. Chem. Intermed.* **2015**, *41*, 9845–9862. [[CrossRef](#)]
39. Biriaei, R.; Halladj, R.; Askari, S. Heavy Metal Ions Uptake by AlPO-5 and SAPO-5 Nanoparticles: An Experimental and Modeling Study. *Water Environ. Res.* **2017**, *89*, 337–347. [[CrossRef](#)]
40. Jaseela, P.K.; Garvasis, J.; Joseph, A. Selective adsorption of methylene blue (MB) dye from aqueous mixture of MB and methyl orange (MO) using mesoporous titania (TiO<sub>2</sub>)—Poly vinyl alcohol (PVA) nanocomposite. *J. Mol. Liq.* **2019**, *286*, 110908. [[CrossRef](#)]
41. Huang, T.; Yan, M.; He, K.; Huang, Z.; Zeng, G.; Chen, A.; Peng, M.; Li, H.; Yuan, L.; Chen, G. Efficient removal of methylene blue from aqueous solutions using magnetic graphene oxide modified zeolite. *J. Colloid Interface Sci.* **2019**, *543*, 43–51. [[CrossRef](#)]
42. Sarah, M.A.; Mohd, R.T.; Omer, M.E.T. Kinetics and isotherms of dichlorodiphenyltrichloroethane (DDT) adsorption using soil–zeolite mixture. *Nanotechnol. Environ. Eng.* **2018**, *3*, 4.

**Disclaimer/Publisher’s Note:** The statements, opinions and data contained in all publications are solely those of the individual author(s) and contributor(s) and not of MDPI and/or the editor(s). MDPI and/or the editor(s) disclaim responsibility for any injury to people or property resulting from any ideas, methods, instructions or products referred to in the content.